

First-principles investigations of the atomic, electronic, and thermoelectric properties of equilibrium and strained Bi_2Se_3 and Bi_2Te_3 including van der Waals interactions

Xin Luo, Michael B. Sullivan, and Su Ying Quek*

Institute of High Performance Computing, Agency for Science, Technology and Research, 1 Fusionopolis Way, #16-16 Connexis, Singapore 138632

(Received 10 July 2012; revised manuscript received 7 November 2012; published 27 November 2012)

Bi_2Se_3 and Bi_2Te_3 are layered compounds of technological importance, being excellent thermoelectric materials as well as topological insulators. We report density functional theory calculations of the atomic, electronic, and thermoelectric properties of strained bulk and thin-film Bi_2Se_3 and Bi_2Te_3 , focusing on an appropriate description of van der Waals (vdW) interactions. The calculations show that the van der Waals density functional (vdW-DF) with Cooper's exchange (vdW-DF^{CO_x}) can reproduce closely the experimental interlayer distances in unstrained Bi_2Se_3 and Bi_2Te_3 . Interestingly, we predict atomic structures that are in much better agreement with the experimentally determined structure from Nakajima than that obtained from Wyckoff, especially for Bi_2Se_3 , where the difference in atomic structures *qualitatively* changes the electronic band structure. The band structure obtained using the Nakajima structure and the vdW-DF^{CO_x} optimized structure are in much better agreement with previous reports of photoemission measurements, than that obtained using the Wyckoff structure. Using vdW-DF^{CO_x} to fully optimize atomic structures of bulk and thin-film Bi_2Se_3 and Bi_2Te_3 under different in-plane and uniaxial strains, we predict that the electronic bandgap of both the bulk materials and thin films decreases with tensile in-plane strain and increases with compressive in-plane strain. We also predict, using the semiclassical Boltzmann approach, that the magnitude of the *n*-type Seebeck coefficient of Bi_2Te_3 can be increased by the compressive in-plane strain while that of Bi_2Se_3 can be increased with tensile in-plane strain. Further, the in-plane power factor of *n*-doped Bi_2Se_3 can be increased with compressive uniaxial strain while that of *n*-doped Bi_2Te_3 can be increased by compressive in-plane strain. Strain engineering thus provides a direct method to control the electronic and thermoelectric properties in these thermoelectric topological insulator materials.

DOI: [10.1103/PhysRevB.86.184111](https://doi.org/10.1103/PhysRevB.86.184111)

PACS number(s): 62.25.-g, 61.50.Lt, 71.15.Nc, 71.20.Mq

I. INTRODUCTION

Bi_2Se_3 and Bi_2Te_3 are members of the $(\text{Bi}, \text{Sb})_2(\text{Te}, \text{Se})_3$ family of traditional thermoelectric materials—they can directly convert waste heat to electricity without any moving parts. These bulk thermoelectric materials were discovered to have large Seebeck coefficients half a century ago and are now widely used in thermoelectric refrigeration.^{1–3} In recent years, there has been a surge of renewed interest in these thermoelectric materials—it was predicted and later, experimentally demonstrated,^{4–7} that these materials constitute an exotic class of condensed matter, called topological insulators.^{8–10} The topological insulators are distinguished by the existence of metallic spin-helical surface states, which are robust against the presence of nonmagnetic impurities or disorder.^{11,12} These surface states have potential applications in spintronics,^{9,13} quantum computation,^{8,10,14} and thermoelectric energy conversion.¹⁵ Importantly, these applications require a better fundamental understanding of the atomic and electronic structure of Bi_2Se_3 and Bi_2Te_3 when interfaced with other materials.

It is well known that Bi_2Se_3 and Bi_2Te_3 belong to the tetradymite-type crystal with a rhombohedral structure (point group $R\bar{3}m$). In the rhombohedral unit cell [Fig. 1(a)], there are three Se (Te) atoms that can be classified into two inequivalent types. We label these inequivalent atoms as $\text{Se}_1(\text{Te}_1)$ (two of them in one unit cell) and $\text{Se}_2(\text{Te}_2)$. The Bi atoms are equivalent. The Bi_2Se_3 and Bi_2Te_3 structure is also often alternatively described in the hexagonal representation with a unit cell of 15 atoms, as shown in Fig. 1(b). Within this

representation, it is clear that Bi_2Se_3 and Bi_2Te_3 have layered structures. Each $\text{Se}_1(\text{Te}_1)$ -Bi- $\text{Se}_2(\text{Te}_2)$ -Bi- $\text{Se}_1(\text{Te}_1)$ forms a so-called quintuple layer (QL), which is a slab with five atomic layers. The QLs are stacked along the *c* axis with the weak van der Waals (vdW) interactions between neighboring QLs. The vdW interaction is relatively weak, but it can play a dominant role in interactions between atoms or layers separated by empty space (so-called sparse matter). This interaction results exclusively from long-range correlations, which are absent from standard local and gradient-corrected density functional theory (DFT) functionals.^{16,17} Much significant advancement has since been made that enables the treatment of vdW interactions within DFT. In addition to the method of dispersion-correction as an add-on to DFT,¹⁸ the recently developed van der Waals density functional (vdW-DF)^{19,20} incorporates the long-range dispersion effects as a perturbation to the local-density approximation (LDA) correlation term, and this method has been applied successfully in diverse material systems.¹⁷ The choice of exchange functional is also important—the standard functional used within vdW-DF, revised Perdew–Burke–Ernzerhof (revPBE)²¹ typically gives vdW bond lengths that are a few percent too large.²² Most recently, Cooper developed an exchange functional that reduces the short-range repulsion term in revPBE.²³

Although extensive electronic structure calculations have been performed for Bi_2Se_3 and Bi_2Te_3 ,^{13,24–31} most of them are calculated with experimental structures without full relaxation or in the slab calculations, with only the top four layers of atoms in the top QL allowed to relax, fixing the inter-QL distance.^{13,32}

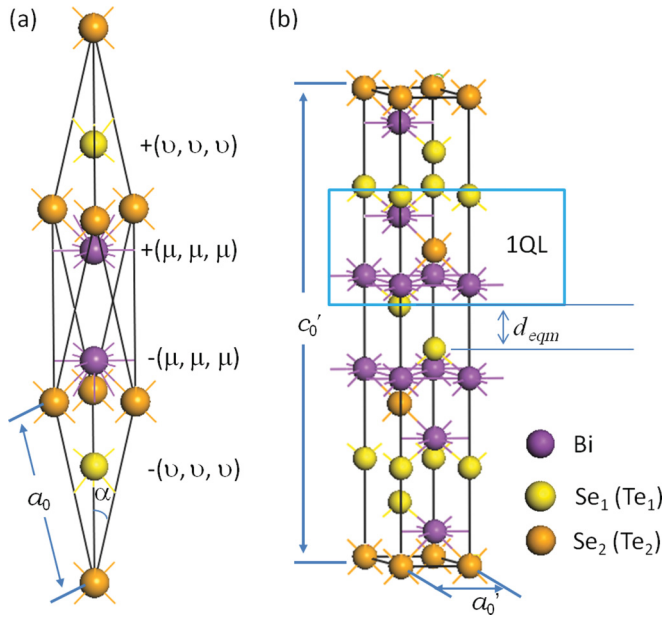


FIG. 1. (Color online) Atomic structures of bulk Bi_2Te_3 and Bi_2Se_3 . One QL contains five atoms in $\text{Se}_1(\text{Te}_1)$ - Bi - $\text{Se}_2(\text{Te}_2)$ - Bi - $\text{Se}_1(\text{Te}_1)$ series. (a) Rhombohedral unit cell. (b) Hexagonal unit cell (containing three QLs)

Yet, inter-QL vdW interactions are essential for predicting atomic and electronic structures of Bi_2Se_3 and Bi_2Te_3 , when interfaced or intercalated with other materials. Indeed, much of the current interest in these materials involves interfacing them with other materials, and recent experiments indicate that depositing Ag on Bi_2Se_3 results in Ag intercalation between QLs.^{11,33} Furthermore, vdW interactions are required for accurate predictions of atomic structures of Bi_2Se_3 and Bi_2Te_3 under strain, which can directly influence topological properties.^{28,34,35} On the other hand, previous theoretical calculations found that pressure and uniaxial stress can greatly influence the thermoelectric properties of Sb_2Te_3 ,³⁶ and stress also plays an important role in the formation of defects in these thermoelectric materials.^{37,38} Recent experiments and molecular simulations show that the lattice thermal conductivity of thermoelectric materials will be affected by different strain conditions.^{39,40} How important is the vdW interaction in strain engineering, and how do they affect the thermoelectric properties of these materials?

In this paper, we first explore the applicability of different exchange-correlation functionals, including those with vdW corrections, on predicting atomic structures of Bi_2Se_3 and Bi_2Te_3 . Next, using an appropriate vdW functional, we fully optimize the atomic structures of strained bulk and thin-film Bi_2Se_3 and Bi_2Te_3 . Based on these optimized reference structures, the effect of strain on atomic, electronic, and thermoelectric properties are reported, and the importance of vdW interactions is elucidated by comparing the results with those obtained using structures optimized with the Perdew–Burke–Ernzerhof (PBE) functional (including spin-orbit interactions). We also explore the effects of vdW interactions and spin-orbit interactions on the bulk moduli and phonon frequencies in the unstrained bulk systems.

II. COMPUTATIONAL DETAILS

Except for the thermoelectric transport properties (addressed below), all our calculations are performed using the plane wave DFT code, Quantum-ESPRESSO (QE).³⁴ The norm-conserving pseudopotentials are generated using the Rappe-Rabe-Kaxiras-Joannopoulos (RRKJ) approach. For structural relaxation, the plane-wave kinetic energy cutoff is set to 56 Ry and the Brillouin zone is sampled with a $9 \times 9 \times 1$ Monkhorst-Pack mesh—using a higher plane-wave cutoff of 70 Ry and a $13 \times 13 \times 1$ k -point mesh changes the lattice constants and internal coordinates by less than 0.2%, with essentially no difference in resulting band structure. Phonon frequencies in the bulk are computed using a dense k -point mesh of $13 \times 13 \times 13$. On the other hand, a plane-wave cutoff of 40 Ry is found to be sufficient (compared to 56 Ry) for calculations of band structure and bulk moduli. A vacuum thickness of 16 Å is used in thin-film slab calculations (converged relative to a vacuum thickness of 20 Å). In the self-consistent calculation, the convergence threshold for energy is set to 10^{-9} eV. All the internal atomic coordinates and lattice constants are relaxed, until the maximum component of Hellmann-Feynman force acting on each ion is less than 0.003 eV/Å. The spin-orbit coupling (SOC) effect, important for the heavy elements considered here, is treated self-consistently in fully relativistic pseudopotentials for the valence electrons.⁴¹ In order to investigate the importance of SOC and vdW interactions for different physical properties, we have performed a detailed investigation with different exchange-correlation functionals. However, the main physical insights are obtained using atomic structures optimized using the vdW-DF functional^{19,20,42} with Cooper’s exchange²³ and electronic structure calculated using the PBE⁴³ functional with SOC.

Many thermoelectric calculations^{44–46} of similar materials are based on the WIEN2k package⁴⁷ with the semiclassical Boltzmann transport method in the relaxation-time approximation.⁴⁸ Therefore, to compare our results with the literature, we use WIEN2k with BoltzTrap⁴⁵ for calculating thermoelectric transport properties of our previously relaxed structures, with the same basis functions as in the reported literature,^{44,45} and using the PBE⁴³ functional with SOC⁴⁹ as implemented in WIEN2k. The calculation of transport properties requires a very dense k grid; here, a nonshifted mesh with 56 000 k points (4960 in the irreducible Brillouin zone) is used, which is found to be converged as compared to a denser sampling with 70 000 k points. Within BoltzTrap, the relaxation time τ is assumed to be a constant with respect to the wave vector k and energy around the Fermi level, and the effect of doping is introduced by the rigid band approximation. Within the relaxation-time approximation, the Seebeck coefficient S can be obtained directly from the electronic structure without any adjustable parameters.

III. RESULTS AND DISCUSSIONS

A. Structural properties of equilibrium Bi_2Se_3 and Bi_2Te_3

Table I shows the fully optimized lattice constants and internal coordinates obtained using different functionals. The different functionals give consistent internal coordinates, but

TABLE I. Structural parameters for Bi_2Se_3 and Bi_2Te_3 . Within the rhombohedral representation, the unit cell is described by the lattice constant a_0 and angle α , the atom $\text{Se}_2(\text{Te}_2)$ is set to be the origin $(0, 0, 0)$, and the two Bi atoms occupy sites $\pm(\mu, \mu, \mu)$, while the two Se(Te) atoms are located at $\pm(\nu, \nu, \nu)$. The corresponding hexagonal cell edge is denoted by a_0' and c_0' , and the equilibrium inter-QL distance (d_{eqm}) in hexagonal cell is also shown (see Fig. 1 for notation).

	Exp. 1 ^a	Exp. 2 ^b	LDA	LDA + SOC	PBE	PBE + SOC	revPBE	PBE-D2	PBE-D2 + SOC	vdW-DF ^{CO9} _x	vdW-DF ^{revPBE} _x
Bi_2Se_3											
a_0 (Å)	9.8405	9.841	9.616	9.552	10.889	10.617	12.458	9.938	9.8774	9.8771	11.18
α (°)	24.304	24.273	24.593	24.8507	22.123	22.792	19.493	23.905	24.152	24.105	21.895
μ (Bi)	0.4008	0.399	0.4009	0.4016	0.3946	0.3959	0.3868	0.3992	0.3998	0.4001	0.3946
ν (Se)	0.2117	0.206	0.2097	0.2081	0.2228	0.2199	0.2369	0.2127	0.2113	0.2115	0.2235
a_0' (Å)	4.143	4.138	4.096	4.111	4.178	4.195	4.218	4.116	4.133	4.125	4.246
c_0' (Å)	28.636	28.64	27.96	27.758	31.86	31.01	36.65	28.95	28.755	28.757	32.72
d_{eqm} (Å)	2.579	2.253	2.406	2.298	3.574	3.302	5.145	2.668	2.570	2.580	3.722
2 QL d_{eqm} ^a (Å)	2.579	2.253	2.380	2.28	3.58	3.38	>4.48	2.68	2.68	2.48	3.58
Bi_2Te_3											
a_0 (Å)	10.476	10.473	10.175	10.124	10.829	10.628	12.399	10.664	10.565	10.368	11.138
α (°)	24.166	24.167	24.574	24.806	23.647	24.223	20.678	23.305	23.703	24.277	23.449
μ (Bi)	0.4000	0.400	0.4004	0.4012	0.3979	0.3996	0.3900	0.3985	0.3990	0.3999	0.3972
ν (Te)	0.2095	0.212	0.2083	0.2063	0.2146	0.2109	0.2294	0.2120	0.2099	0.2094	0.2168
a_0' (Å)	4.386	4.384	4.331	4.349	4.438	4.460	4.450	4.308	4.340	4.360	4.527
c_0' (Å)	30.497	30.487	29.589	29.423	31.565	30.934	36.390	31.109	30.792	30.174	32.48
d_{eqm} (Å)	2.612	2.764	2.466	2.331	3.025	2.736	4.566	2.822	2.651	2.582	3.259
2 QL d_{eqm} ^c (Å)	2.612	2.764	2.41	2.31	3.11	2.81	>4.31	2.71	2.71	2.51	3.41

^aFrom Ref. 58 (Nakajima).

^bFrom Ref. 59 (Wyckoff).

^c d_{eqm} for 2 QL is obtained from Fig. 2.

the lattice parameters, especially that related to the interlayer distance d_{eqm} (vertical distance between Se (or Te) atoms in adjacent QLs), vary significantly with different functionals. Focusing first on the LDA, PBE, and revPBE functionals, we find that LDA⁵⁰ results are closest to experiment, with LDA underestimating d_{eqm} by 6.7 and 5.6% for Bi₂Se₃ and Bi₂Te₃, respectively, and PBE⁴³ overestimating d_{eqm} by 38.6 and 15.8% for Bi₂Se₃ and Bi₂Te₃, respectively. The revPBE²¹ functional predicts an even larger d_{eqm} of >4.48 Å. Calculations with the vdW-DF correlation functional together with revPBE exchange lead to improved, smaller d_{eqm} compared to the revPBE functional; however, the predicted d_{eqm} is still overestimated by more than 20%. This error is much larger than that reported for other vdW-bonded systems.²² In contrast, the semiempirical vdW correction based on Grimme's scheme (PBE-D2)^{18,51,52} does help, predicting d_{eqm} within 3.4 and 8% of experiment for Bi₂Se₃ and Bi₂Te₃, respectively. On the other hand, using the vdW-DF functional^{19,53} with the most recently developed Cooper's exchange (vdW-DF^{CO₉_x}),²³ we can obtain better agreement with experiment, with predicted d_{eqm} values of 2.58 Å for Bi₂Se₃ and 2.582 Å for Bi₂Te₃, which are within 0.1 and 1.1% of experiment. We next consider the role of SOC in relaxing atomic structures. We find that SOC tends to reduce d_{eqm} in all cases; as a result, adding SOC increases the error for LDA but reduces the error for PBE and PBE-D2, thus giving d_{eqm} values within 1.5% of experiment for PBE-D2 + SOC. As the vdW-DF functional has not been implemented with SOC, we did not check the effect of SOC on these results. However, since vdW-DF^{CO₉_x} can already give excellent agreement with experiment, it is still unclear if SOC is truly important for structural optimization. We note that the very reasonable results of PBE-D2 and PBE-D2 + SOC are quite remarkable given that the correction is semiempirical. However, in the following, we shall base most of our conclusions on structures optimized using the vdW-DF^{CO₉_x} functional.

Since the interlayer vdW interactions are important, we focus on these interactions by computing, for simplicity, the inter-QL binding energy as a function of interlayer distance, for two QL Bi₂Se₃ and Bi₂Te₃ thin films (i.e., films with two QLs each containing five atomic layers), where the internal atoms within each QL are fixed to their experimental atomic positions from the bulk (Fig. 2). Although the inter-QL distance for the two-QL film may be slightly different from the bulk, it has been shown that the vdW interactions are dominated by those between nearest-neighbor layers in other layered materials such as multilayer graphene and MoS₂.^{54,55} The close correspondence (with deviation of less than 5% for all functionals) between the equilibrium inter-QL distances calculated for the bulk and for two QLs (Table I) further supports this assumption. From Fig. 2, we see that revPBE and revPBE + SOC give rise to repulsive interactions between the two QLs. Furthermore, the curvature of the energy versus distance curve is quite different for different functionals. Although SOC does not change d_{eqm} significantly, it does affect the interlayer force constants, which are given by the second derivative of the energy as a function of distance. We also note that the binding energies obtained using vdW-DF^{CO₉_x} or PBE-D2 are consistent with recent estimates obtained by rescaling results from the VV10 functional⁵⁶ according to quantitative random-phase approximation (RPA)

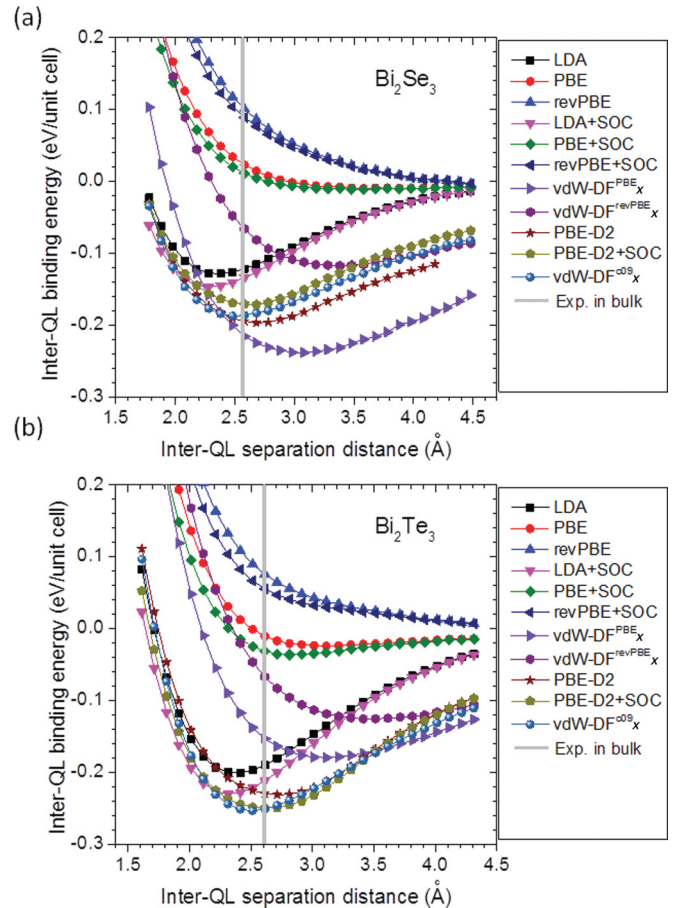


FIG. 2. (Color online) Inter-QL binding energy as a function of inter-QL separation distance for (a) Bi₂Se₃ and (b) Bi₂Te₃ two-QL thin films. The inter-QL energy is computed by taking the difference between the total energy of the two-QL film and twice that of a one QL film in the same unit cell. Here, the internal atoms within each QL are fixed to their experimental atomic positions from the bulk. The grey line shows the value of experimental distance in bulk, which is from Ref. 58.

calculations.⁵⁷ These binding energies are larger for Bi₂Te₃ than for Bi₂Se₃, a finding consistent with the larger atomic size of Te compared to Se.

Interestingly, we find that our first-principles-predicted structures using both PBE-D2 and vdW-DF^{CO₉_x} functionals are more consistent with the experimental structures reported by Nakajima,⁵⁸ rather than that from Wyckoff (Table I).⁵⁹ Both experimental structures have been widely used in the theoretical literature, but importantly, the internal atomic coordinates are different in these two structures (Table I), especially for Bi₂Se₃, where the interlayer distance d_{eqm} is quite different (2.579 Å in Nakajima's structure and 2.253 Å in Wyckoff's structure). It is noted that the crystal structure from Wyckoff is obtained from an early electron diffraction study,⁶⁰ while structures of Nakajima are obtained from x-ray diffraction powder analysis. As the interaction of electrons with matter are about 10 000 times stronger than that of xrays, multiple dynamical scattering will influence the intensity of electron diffraction patterns, thus making the structure

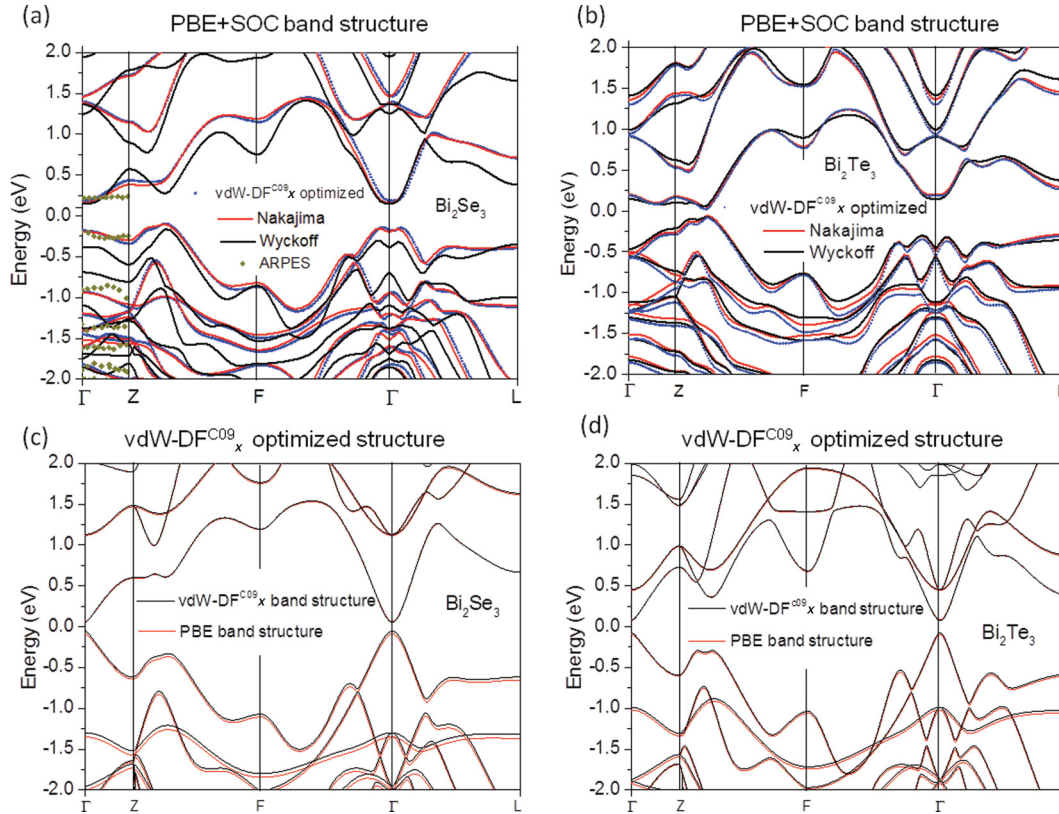


FIG. 3. (Color online) Band structures of bulk (a) Bi_2Se_3 and (b) Bi_2Te_3 , computed using the GGA-PBE functional with SOC. The experimental ARPES data for Bi_2Se_3 (Ref. 61) is shown along the Γ and Z high-symmetry direction. The band structures of (c) Bi_2Se_3 and (d) Bi_2Te_3 without SOC are also calculated with $\text{vdW-DF}^{\text{C09}}_x$ and PBE functionals.

determination from electron diffraction more difficult and less reliable than that from x-ray diffraction.⁵⁸

B. Electronic properties of equilibrium Bi_2Se_3 and Bi_2Te_3

Using PBE + SOC, we compute the band structures of the Nakajima and Wyckoff atomic structures and the $\text{vdW-DF}^{\text{C09}}_x$ optimized structures. We find that the band structures for the $\text{vdW-DF}^{\text{C09}}_x$ optimized structures match very well to those of the Nakajima structures, as we expect from the above discussion. The band structures of the Wyckoff and Nakajima structures are very similar in the case of Bi_2Te_3 [Fig. 3(b)] but are *qualitatively* different for Bi_2Se_3 [Fig. 3(a)]. Focusing now on these differences for Bi_2Se_3 , we note that the lowest conduction band along the Γ -Z-F high-symmetry direction is more rippled in the Wyckoff structure than in the Nakajima and $\text{vdW-DF}^{\text{C09}}_x$ optimized structures [Fig. 3(a)]. Furthermore, the direct gap at F is 0.40 eV smaller in the Wyckoff Bi_2Se_3 structure than in the Nakajima structure, while the bandgap at Γ is 0.20 eV smaller in the Nakajima Bi_2Se_3 structure than in the Wyckoff structure. (We note that the calculated band structures of Bi_2Se_3 based on the PBE-D2 + SOC relaxed structure and that of $\text{vdW-DF}^{\text{C09}}_x$ optimized structures are almost the same; not shown here.) Comparing the computed band structure with that measured in recent angle-resolved photoelectron spectroscopy (ARPES) experiments,⁶¹ we find that the band structure for the Nakajima structure is closer to experiment than that for the Wyckoff structure, thus providing

direct experimental evidence favoring the coordinates from Nakajima and our optimization procedure. Specifically, there are two key qualitative features indicating that the ARPES measurements agree better with the band structure for the Nakajima structure. Focusing on the band structure along Γ -Z, close to the Fermi level, we see (1) the highest-occupied valence band is flatter in the Nakajima structure, similar to that from ARPES; (2) the energy separation between the highest-occupied valence band and the next-highest-occupied band is about 0.75 eV for the Nakajima structure, in contrast to 0.3 eV for the Wyckoff structure and similar to that from ARPES. It is thus clear that agreement is much better for the Nakajima structure than for the Wyckoff structure. Interestingly, the authors of the ARPES paper⁶¹ had commented that the measured energy bands in the Γ -Z direction were significantly flatter than that predicted by DFT; our calculations strongly suggest that the reason for this discrepancy was that the Wyckoff structure was used for their calculations instead of the Nakajima structure. Since the main difference between the Nakajima and Wyckoff Bi_2Se_3 structures is the larger interlayer separation in the former, these results underscore the importance of a careful treatment of vdW interactions for prediction of band structures.

We note that although DFT in many cases gives accurate qualitative predictions of band structure, the DFT Kohn-Sham values cannot quantitatively predict quasiparticle band structures.⁶² In this case, the calculated bandgaps of Bi_2Se_3 and Bi_2Te_3 (using the $\text{vdW-DF}^{\text{C09}}_x$ optimized structures) are 0.30

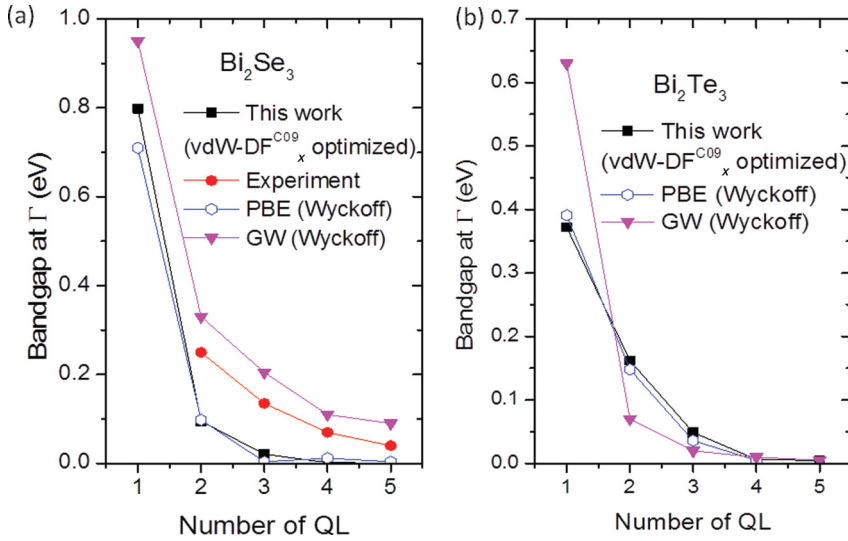


FIG. 4. (Color online) Thickness-dependent bandgaps at the Γ point induced by the interaction between the surface states of thin film for (a) Bi_2Se_3 and (b) Bi_2Te_3 . Experimental results are reproduced from Ref. 66, PBE data are obtained from Ref. 65, and the GW calculation data are derived from Ref. 64. The slab structures in PBE and GW calculations are based on the Wyckoff structures.

and 0.10 eV, slightly smaller than the experimentally measured values of 0.35 eV for Bi_2Se_3 ⁶³ and 0.17 eV for Bi_2Te_3 ⁶ but consistent with the other DFT results.^{13,26}

Although our calculations suggest that SOC is not crucial for predicting atomic structures, SOC has an important effect on the band structure. To illustrate this, we compare the band structures in Figs. 3(a) and 3(b) with those computed without SOC [Figs. 3(c) and 3(d)], using the vdW-DF^{C09}_x optimized structures. The band structures with and without SOC are quite different, consistent with large SOC-induced band inversion at Γ . Furthermore, we note that the band structures computed by the vdW-DF^{C09}_x functional and PBE are quite similar, suggesting that the vdW-DF^{C09}_x functional can produce band structures that are consistent with PBE and that vdW interactions have minimal effect on the band structure. This justifies our neglect of vdW effects in the band structure calculations.

Recent interest in the topological metallic surface states in Bi_2Se_3 and Bi_2Te_3 slabs focus on the Dirac cone feature in the band structure at the Γ point.^{13,30,64–66} At very thin slab thickness, the interaction between the surface states at opposite interfaces opens the bandgap at Γ , and this gap will gradually decay to zero as the slab thickness is increased. Previous PBE (with SOC) calculations on the unrelaxed slabs derived from Wyckoff structures found that the bandgap at Γ begins to close by three and four QLs for Bi_2Se_3 and Bi_2Te_3 , respectively.⁶⁵ To address the question of whether the atomic structure influences these predictions, we fully optimized slab structures from one to five QLs using the vdW-DF^{C09}_x functionals; the fully optimized slab structures are similar to those directly derived from Nakajima structures. Based on the optimized slab structures, we calculated the bandgap at Γ with PBE + SOC, as shown in Fig. 4. Our results are close to that using the Wyckoff structures, except that the bandgap closes only at four QLs instead of three QLs for Bi_2Se_3 . We note that compared to experiment and previous GW calculations,⁶⁴ the predicted gaps are too small. It is unclear if using the Nakajima instead of the Wyckoff structures would affect the computed GW gaps; however, such calculations are beyond the scope of the current work.

C. Bulk moduli and phonon frequencies of equilibrium Bi_2Se_3 and Bi_2Te_3

We further predict the bulk moduli and phonon frequencies of equilibrium Bi_2Se_3 and Bi_2Te_3 with vdW-DF^{C09}_x and other functionals and compare our predictions with available experimental literature. The bulk modulus B and its pressure derivative B' can be obtained by computing the changes in total energy of Bi_2Se_3 and Bi_2Te_3 with hydrostatic pressure and fitting the resulting energy-volume curves using the Birch-Murnaghan equation of state:

$$E(\eta) = E_0 + \frac{9BV_0}{16} [(\eta^2 - 1)^3 B' + (\eta^2 - 1)^2 (6 - 4\eta^2)], \quad (1)$$

where $\eta = (V_0/V)^{1/3}$, V_0 is the equilibrium volume of the fully relaxed structure. The bulk moduli thus obtained are reported in Table II. In general, the values of B predicted for both Bi_2Se_3 and Bi_2Te_3 are similar (~ 30 – 40 GPa). The experimental reports for B differ, especially for Bi_2Se_3 , where an exceptionally high value of 53 GPa is obtained by Vilaplana *et al.*⁶⁷ However, the remaining experimental values are in reasonable agreement with our predicted values. Due to the different experimental values, we are unable to draw a conclusion of the importance of vdW interactions or SOC in determining the bulk modulus.

More insights can be obtained by comparing computed zone center phonon frequencies with experiment. As can be shown by group theory, the irreducible representations of the zone center phonon modes in Bi_2Te_3 and Bi_2Se_3 are $\Gamma = 2A_{1g} + 3A_{2u} + 2E_g + 3E_u$, among which $2A_{1g}$ and $2E_g$ are Raman (R) active; $3A_{2u}$ and $3E_u$ are infrared (I) active, the three acoustic modes are composed by one A_{2u} and two degenerate E_u modes. For the R-active modes, E_g describes the shear mode of in-plane atomic vibrations, and A_{1g} describes the breathing mode of out-of-plane atomic vibrations. Except for results obtained with the vdW-DF functional, all phonon frequencies are computed within density functional perturbation theory (DFPT) as introduced by Lazzeri and Mauri⁶⁸ in QE. Since the phonon frequencies cannot be

TABLE II. The calculated bulk moduli B (GPa) of Bi_2Te_3 and Bi_2Se_3 .

	vdW-DF ^{C09} _x	PBE-D2	PBE-D2 + SOC	LDA	LDA + SOC	PBE + SOC	Exp.
Bi_2Se_3	42.8	42.92	41.0	46.68	48.82	49.45	32.98 ^a , 53 ^b
Bi_2Te_3	40.2	35.61	32.5	42.46	46.56	42.55	39.47 ^c , 32.5 ^d

^aFrom Ref. 81.^bFrom Ref. 67.^cFrom Ref. 82.^dFrom Ref. 83.

computed with vdW-DF in QE, we adopt the force-constant approach^{69,70} to compute the phonon frequencies with the vdW-DF^{C09}_x functional. In this method, we displace each atom in the primitive cell from its equilibrium position in the x , y , and z directions by a distance of 0.015 Å and calculate the forces acting on each atom using the Hellmann-Feynman theorem. Subsequently, the interatomic force-constant matrix is evaluated using a central finite-difference scheme. (We have checked that within LDA, the phonon frequencies as calculated with the force-constant approach are essentially the same as those obtained from the DFPT method.)

First, comparing LDA and PBE results with and without SOC with experiment (Table III), we note that in all cases, SOC reduces the phonon frequencies. In general, inclusion of SOC then leads to better agreement with experiment, as previously observed by Cheng *et al.*⁷¹ We note that the importance of SOC in determining force constants is in contrast to our earlier observation that SOC was not important for structural relaxation. The difference lies in the fact that force constants are related to the rate of change of force with atomic displacements, whereas structural relaxation is related only to the coordinates for the

minima of the potential energy surface. This can be illustrated in the simplified picture in Fig. 2 where the minima of the energy-distance curves are similar with and without SOC, but the curvatures of the curves are quite different. Next, although the PBE atomic structure is significantly different from experiment compared to the PBE-D2 atomic structure, we find that the PBE frequencies are quite similar to the PBE-D2 frequencies, and in fact, the PBE-D2 frequencies are in many cases slightly farther from the experimental values. The PBE-D2 frequencies are quite similar to those obtained with the vdW-DF^{C09}_x functional. However, PBE-D2 + SOC frequencies give the best match with experiment, suggesting that PBE-D2 + SOC can be used to make predictions on frequencies.

D. Atomic and electronic properties of strained Bi_2Se_3 and Bi_2Te_3

Strain engineering is a mature technique for controlling the electronic properties of nanoscale semiconductors in industry—mechanical strain can be imposed by microelectromechanical systems (MEMS) or by epitaxial growth of thin

TABLE III. Calculated zone-center phonon frequencies for Bi_2Se_3 and Bi_2Te_3 bulks with and without SOC and the unit of frequency is in wave number per centimeter. The R- and I-active modes are denoted with R or I.

		LDA + SOC	LDA	PBE + SOC ^a	PBE ^a	PBE-D2 + SOC	PBE-D2	vdW-DF ^{C09} _x	Exp.
Bi_2Se_3	E_g^1 (R)	42.80	44.272	38.893	42.128	38.83	43.92	43.048	37 ^b
	A_{1g}^1 (R)	75.50	74.978	63.843	74.584	71.58	74.94	72.639	72.2 ^c
	E_u^1 (I)	82.46	86.966	64.677	85.057	83.92	89.33	86.288	
	E_u^2 (I)	131.06	136.108	126.819	132.957	128.80	135.23	133.62	131.4 ^c
	E_g^2 (R)	137.99	142.911	123.984	138.894	130.47	138.39	138.172	
	A_{2u}^1 (I)	137.44	145.20	136.692	142.730	146.67	153.36	146.575	
	A_{2u}^2 (I)	162.89	171.504	155.439	167.113	165.87	169.95	167.856	
Bi_2Te_3	A_{1g}^2 (R)	174.46	180.546	166.346	179.455	175.47	182.80	179.762	174 ^c
	E_g^1 (R)	42.04	43.34	35.457	36.358	38.51	41.84	40.737	34.356 ^d
	A_{1g}^1 (R)	62.64	65.6	53.869	53.903	59.99	61.54	62.184	62.042 ^d
	E_u^1 (I)	64.28	69.4	48.399	63.142	66.77	76.18	68.945	
	E_u^2 (I)	94.92	99.65	91.228	97.399	95.46	102.68	100.393	
	E_g^2 (R)	104.67	112.72	95.931	104.404	102.75	111.19	109.670	101.735 ^d
	A_{2u}^1 (I)	96.8	104.03	95.064	102.569	104.30	111.89	103.956	
	A_{2u}^2 (I)	120.5	129.47	118.613	128.220	126.81	137.21	128.644	
	A_{1g}^2 (R)	131.91	140.38	127.219	137.2266	136.45	145.83	139.788	134.091 ^d

^aPBE + SOC and PBE calculated data cited from Ref. 71.^bReference 84.^cReference 67.^dReference 85.

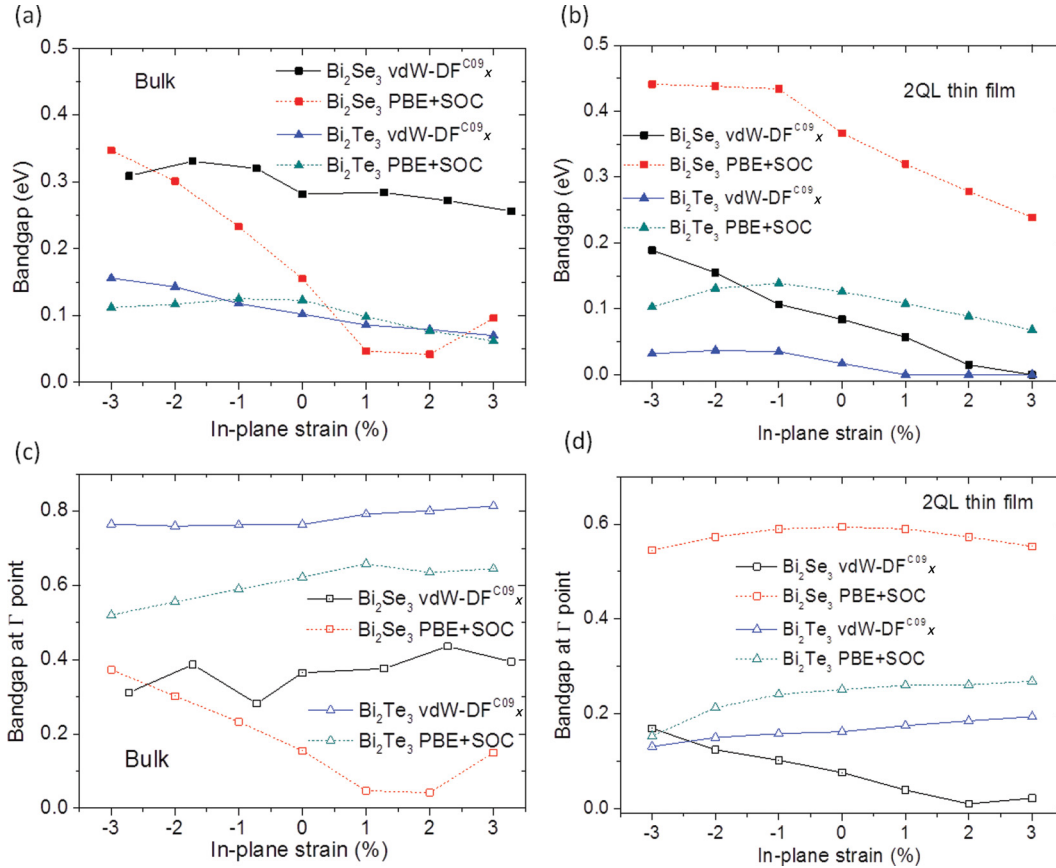


FIG. 5. (Color online) (a) and (b) Calculated bandgap as a function of in-plane strain applied to Bi_2Se_3 and Bi_2Te_3 (a) bulk materials and (b) two-QL thin films. (c) and (d) Bandgap at Γ point as a function of in-plane strain for (c) bulk and (d) two-QL thin films. All band structures are calculated by PBE + SOC; the notation behind each material denotes which functional is used to relax the structure.

films. To study the effect of strain on the atomic structures and electronic properties of Bi_2Se_3 and Bi_2Te_3 , we imposed different in-plane and uniaxial strains to the bulk material. The strain is defined by $\eta = (\alpha_{\text{strain}}/\alpha_0 - 1) \times 100\%$, where α_{strain} is the lattice constant of the strained state, and α_0 is the optimized lattice constant of the unstrained bulk material. α is the in-plane lattice constant and out-of-plane lattice constant for in-plane strain and uniaxial strain, respectively. In our calculation, a uniform in-plane strain from -3 to 3% is applied to Bi_2Se_3 and Bi_2Te_3 bulk and two-QL thin films. For the bulk material, the effect of uniaxial strain from -6 to 6% is also investigated. To predict the strained structures in the bulk, we start by constraining the in-plane (or out-of-plane) lattice constants to the strained state and then relaxing the lattice constant along the c axis (or uniformly in-plane), as well as the internal coordinates, with the vdW-DF^{C09}_x functional. Once we obtain the optimized atomic structures, we compute the electronic properties using PBE + SOC.

With the in-plane strain changing from 3 to -3% , we find that the out-of-plane lattice constants of the relaxed bulk structures increase approximately linearly, with a slope of 0.342 \AA (1.2% of out-of-plane lattice constant) and 0.353 \AA (1.17% of out-of-plane lattice constant) per unit decrease in percentage in-plane strain, for Bi_2Se_3 and Bi_2Te_3 , respectively. For uniaxial strain changing from 6 to -6% , a similar linear relationship was found, with the slope of 0.008 \AA

(0.19% of in-plane lattice constant) and 0.012 \AA (0.27% of in-plane lattice constant) per unit decrease in percentage uniaxial strain for Bi_2Se_3 and Bi_2Te_3 , respectively. These results show that the out-of-plane lattice constant is strongly coupled with the in-plane lattice constant when the structures are optimized under different strain. The different percentage changes suggest strong anisotropy in the elastic properties of these layered materials. Although the overall band structures of the strained systems are similar to those of the unstrained ones, the band structure near the Fermi level is influenced by the applied strains, resulting in significant changes in the bandgaps. Figure 5(a) shows the evolution of bandgap as a function of the in-plane strain for bulk Bi_2Se_3 and Bi_2Te_3 . Focusing on the vdW-DF^{C09}_x relaxed structures, we note that the energy gap increased from 0.07 to 0.16 eV for bulk Bi_2Te_3 , when the in-plane strain changed from 3 to -3% . For vdW-DF^{C09}_x optimized bulk Bi_2Se_3 , the bandgap in general increases from extensive to compressive strain [from 0.25 eV (3.2% strain) to 0.33 eV (-1.8% strain)]. However, further increase in compressive strain to -2.8% reduces the bandgap (here, the k point for the valence-band maximum shifts from its original location near the Z symmetry point to the shoulder of the M shape band near the Γ high-symmetry point). To illustrate the importance of vdW interactions, we relaxed the structures with both vdW-DF^{C09}_x and PBE + SOC functionals and then calculated the electronic structures with PBE + SOC.

The bandgaps for the PBE+SOC optimized bulk Bi_2Te_3 are similar to those for the vdW-DF^{C09}_x relaxed structures. However, the bandgaps obtained for PBE+SOC optimized bulk Bi_2Se_3 are significantly different. These results are consistent with the fact that PBE+SOC overestimates d_{eqm} by 28% in bulk Bi_2Se_3 , but by only 4.7% in bulk Bi_2Te_3 .

Moving now to the two-QL thin films, optimized using vdW-DF^{C09}_x, we note that the optimized in-plane lattice constants are smaller than the bulk—about 0.3 and 1.0% smaller for Bi_2Te_3 and Bi_2Se_3 , respectively. However, the equilibrium inter-QL distances (d_{eqm} is 2.589 Å for Bi_2Se_3 and 2.595 Å for Bi_2Te_3 in the fully relaxed two-QL thin films) are similar to those obtained in Fig. 2. The bandgap for two-QL films is smaller than that for the bulk, because the bandgap in two-QL films is determined by interactions between metallic surface states on both sides of the film. As observed for the bulk, the bandgap for the two-QL films increases with compressive strain and decreases with tensile strain, with the exception of Bi_2Te_3 thin films, where there is a very small decrease in bandgap at -3% compressive strain [Fig. 5(b)]. Further, the Bi_2Se_3 and Bi_2Te_3 thin films become metallic when the tensile strain is larger than 3 and 1%, respectively. We note that in this case, using the PBE+SOC relaxed structures results in bandgaps that are about twice as large or more, although the general trend of how the bandgap evolves with strain are consistent with those for the vdW-DF^{C09}_x optimized structures.

It should be noted that in both the thin films and bulk material, the bandgap is indirect. The direct bandgap at the Γ point is an important issue for topological insulators, because of the Dirac cones at Γ for the thin films. Figures 5(c) and 5(d) show the bandgaps at Γ for both the bulk and the two-QL thin film. We note that Bi_2Se_3 has a smaller direct bandgap at Γ than Bi_2Te_3 but has a larger indirect bandgap; this explains why Bi_2Se_3 is more widely studied for its potential applications as a topological insulator, where it is important to distinguish metallic surface-state carriers from intrinsic bulk carriers. Except for Bi_2Se_3 two-QL films, the direct bandgap at Γ tends to decrease from extensive to compressive strain. Predictions using PBE+SOC relaxed structures result in similar trends for Bi_2Te_3 but not for Bi_2Se_3 .

We note that Young *et al.* has investigated the evolution of the topological phase of bulk Bi_2Se_3 under mechanical strain,²⁸ using regression fits to obtain bandgap stress and stiffness tensors (the linear and quadratic coefficients relating the Γ -point bandgap to strain). From these tensors, it was predicted that the topological phase transition will occur at 6.4% uniaxial strain in the out-of-plane direction, relative to the experimental structure. Here, we apply uniaxial strains on bulk Bi_2Se_3 and Bi_2Te_3 , in each case fully optimizing the internal coordinates and in-plane lattice constants using the vdW-DF^{C09}_x functional. In contrast to the case of in-plane strain, which affects the out-of-plane lattice constant significantly, out-of-plane uniaxial strain has much less effect on the in-plane lattice constant. In general, the gaps decrease with increasing tensile uniaxial strain [Fig. 6(a)], and there is no clear quadratic or linear relation of the uniaxial strain at Γ -point bandgap in Bi_2Se_3 . Our calculations also predict a topological phase transition (closing of Γ -point bandgap) at 6% uniaxial strain for Bi_2Se_3 [Fig. 6(b)], which interestingly, is approximately consistent with the prediction by Young *et al.*

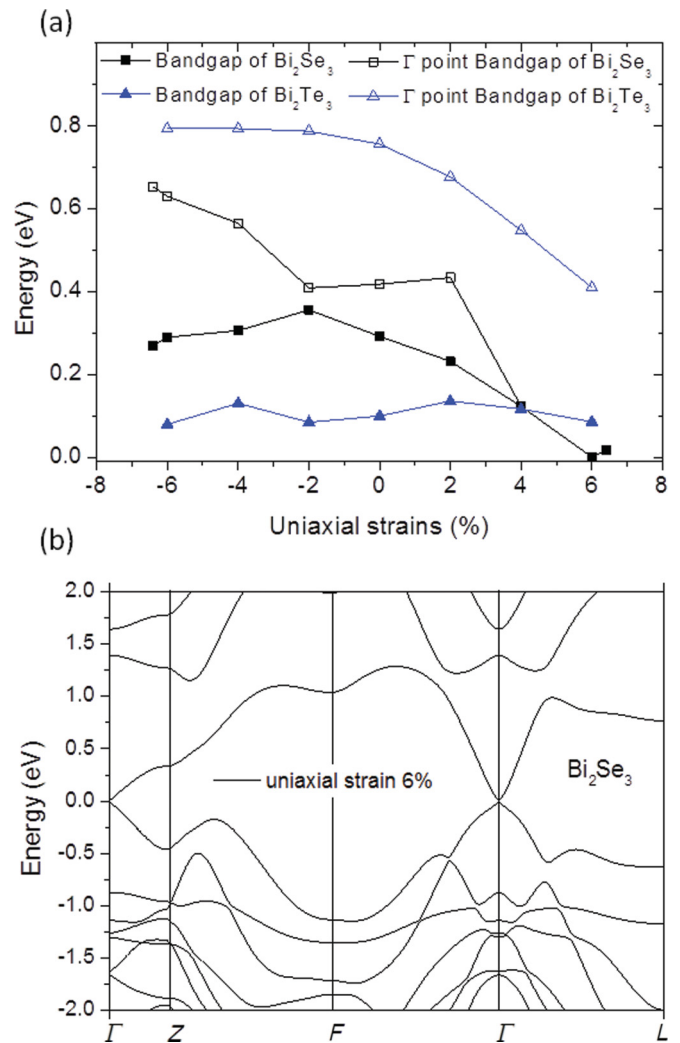


FIG. 6. (Color online) (a) Direct bandgap at Γ point as a function of uniaxial strain in bulk Bi_2Se_3 and Bi_2Te_3 . (b) The topological phase transition at 6% uniaxial strain for Bi_2Se_3 .

Finally, we note that the Γ -point bandgap is more sensitive to uniaxial strain than the indirect bandgap.

To assess the practical feasibility of strain engineering, we compare the strain energy (the energy differences between the strained states and their corresponding unstrained counterparts) with the vdW interaction energy. The strain energy is hundredths of electron volts per unit cell, and even at 3% in-plane strain or 6% uniaxial strain, is still less than 0.1 eV/unit cell. This is quite small compared to the vdW inter-QL interaction energy of about 0.20–0.25 eV/unit cell (Fig. 2), indicating that these layered compounds are likely to be able to withstand such strains without surface exfoliation, the prospects of using strain (e.g., via MEMS) to engineer their bandgaps are promising.

E. Thermoelectric properties

As mentioned before, Bi_2Te_3 and Bi_2Se_3 are traditional thermoelectric materials that can generate electricity from waste heat once a temperature gradient exists.^{46,72–74} The thermoelectric performance is quantified by the figure of merit,

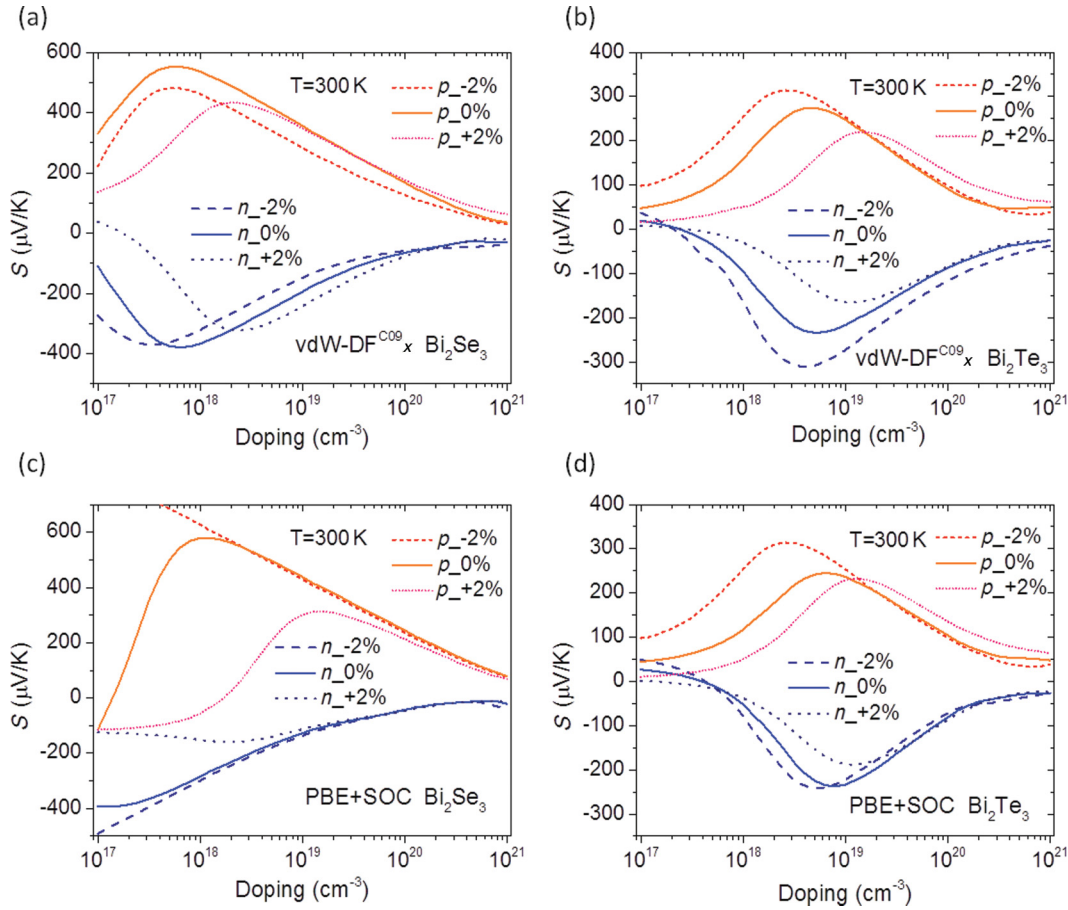


FIG. 7. (Color online) (a) and (b) The Seebeck coefficient S of vdW-DF^{C09}_x optimized, bulk (a) Bi₂Te₃ and (b) Bi₂Se₃ as a function of dopant concentrations, with different in-plane strains. (c) and (d) For comparison, the results based on the PBE + SOC relaxed structure are shown in (c) and (d) for Bi₂Te₃ and Bi₂Se₃, respectively. Please note that the scales are different for the different panels.

ZT , where T is the temperature and Z is defined by³

$$Z = \frac{S^2 \sigma}{(\kappa_e + \kappa_L)}, \quad (2)$$

and S is the Seebeck coefficient, σ the electronic conductivity, and κ_e and κ_L are the electronic and lattice thermal conductivities, respectively. $S^2 \sigma$ is also known as the power factor. Superlattice materials based on Bi₂Te₃ have resulted in high ZT values > 1 .³ A higher ZT can be obtained by increasing the power factor and decreasing the thermal conductivity.⁷⁵ In the following, we shall focus on analyzing the effect of strain on the power factor and the Seebeck coefficient, which can be computed within the linear response regime in the semiclassical Boltzmann framework,⁴⁵ as

$$\sigma \equiv q^2 L_0 \quad (3)$$

$$S = \frac{k_B L_1}{q L_0} \quad (4)$$

with

$$L_j = \int_{-\infty}^{\infty} -\frac{\partial f_0}{\partial E} D(E) v^2 \tau \left(\frac{E - \mu}{k_B T} \right)^j dE,$$

where q is the charge of carriers, f_0 is the Fermi distribution function of electrons, v is the Fermi velocity, τ is the relaxation time, μ is the chemical potential, and $D(E)$ is the density of

states. Using a constant relaxation-time approximation, the Seebeck coefficient can be completely determined from the band structure.

We note that several scholars have done some pioneering thermoelectric studies on related materials, using PBE + SOC optimized structures or experimental structures.^{36,44} It was shown that the semiclassical Boltzmann transport method within the relaxation-time approximation can predict thermoelectric properties of unstrained Bi₂Te₃, in good agreement with experiment.⁴⁴ Furthermore, it was predicted that strain engineering can increase the power factor in Sb₂Te₃.^{36,38} More recently, studies on Bi and Sb tellurides show that the lattice constants and volume expansion have an important influence on the temperature behavior of Seebeck coefficient,⁷⁶ and strain can also play an important role in the anisotropy of electrical conductivity and Seebeck coefficient.⁷⁷ Since most of these studies are carried out in WEIN2k using the semiclassical Boltzmann transport method,⁴⁵ for the sake of comparison, we use the same method (and the same, tested parameters from the literature⁴⁴) for calculation of thermoelectric properties.⁷⁸

We study the effect of in-plane and out-of-plane strain on the in-plane Seebeck coefficient and power factor of bulk Bi₂Se₃ and Bi₂Te₃ under n - and p -type doping, and at different temperatures, using the vdW-DF^{C09}_x optimized structures.

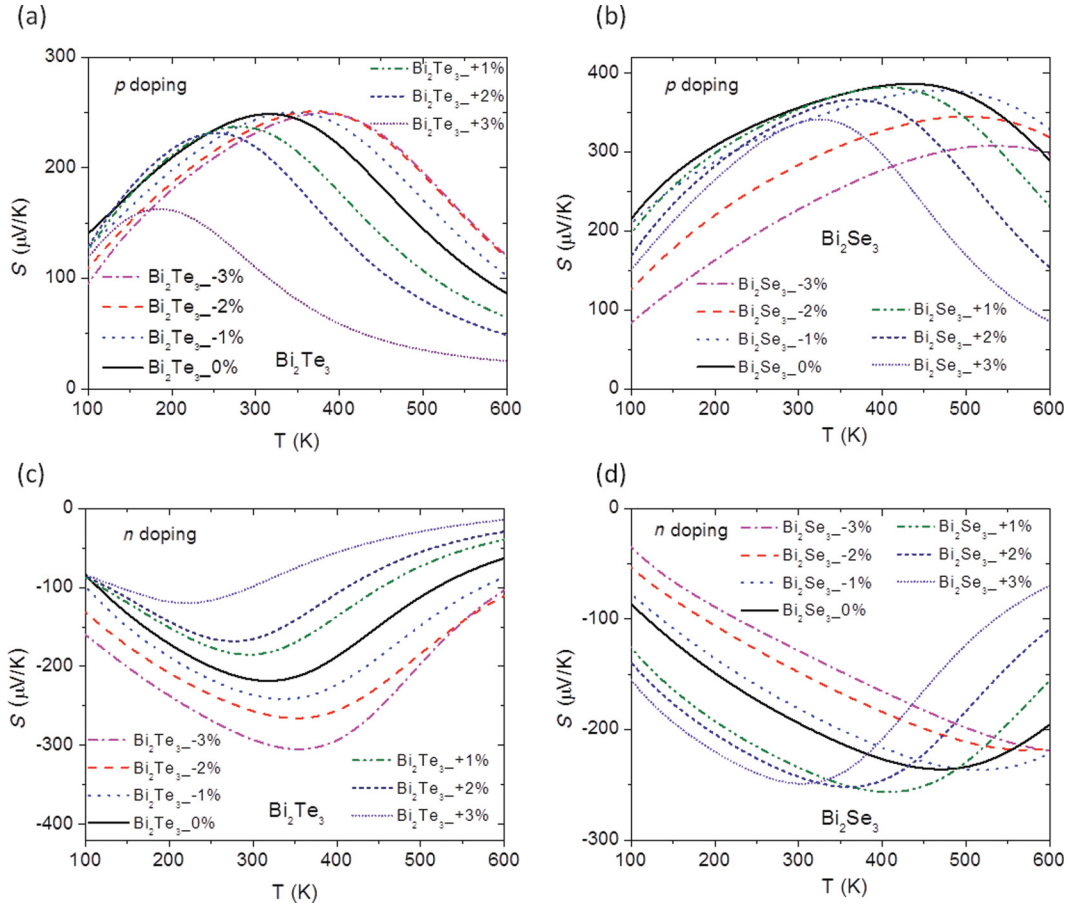


FIG. 8. (Color online) Seebeck coefficient S of Bi_2Te_3 and Bi_2Se_3 under various strained states and both p -type doping and n -type doping are shown. The doping level is fixed to 10^{19}cm^{-3} . Please note that the scales are different for different panels.

(The out-of-plane conductivity is very low, thus resulting in very small out-of-plane power factors.) We find that in-plane compressive strain can significantly improve the Seebeck coefficient and power factor of Bi_2Te_3 (by as much as two times), while effects on Bi_2Se_3 are less significant. Overall, Bi_2Te_3 has a power factor that is an order of magnitude larger than that of Bi_2Se_3 , even in the unstrained state; therefore, these results are significant for further enhancing the ZT of this excellent thermoelectric material. In contrast, we find that uniaxial strain does not improve the power factor of Bi_2Te_3 . For Bi_2Se_3 , the power factor can be increased by compressive uniaxial strain in the case of n doping and by 6% uniaxial tensile strain in the case of p doping.

Figure 7 shows the calculated in-plane Seebeck coefficient S at 300 K for both n -type and p -type doping as a function of carrier concentration. As the electron concentration increases, the Fermi level is shifted higher into the conduction band, resulting in less asymmetry between electrons and holes, therefore reducing the n -type Seebeck coefficient. Similar arguments can be made for p -doped systems. Focusing on the vdW-DF^{C09}_x relaxed structures [Figs. 7(a) and 7(b)], we see that the Seebeck coefficient of p -doped Bi_2Te_3 can be increased by 2% tensile strain for hole concentrations of $10^{19} - 10^{21}\text{cm}^{-3}$ and by 2% compressive strain for hole concentrations of $10^{17} - 10^{19}\text{cm}^{-3}$. On the other hand, 2% compressive strain can increase the magnitude of S in n -doped

Bi_2Te_3 for all dopant concentrations studied, while 2% tensile strain reduces the magnitude of S . This trend is consistent with the increase in bandgap from tensile to compressive strain in Bi_2Te_3 , as well as to the steeper slope of conductivity versus energy [as can be inferred from Fig. 9(b)]. For p -doped Bi_2Se_3 , the overall Seebeck coefficient is significantly higher than Bi_2Te_3 due to the steeper variation of the density of states in the valence bands,⁴⁶ and the effect of strain on the improvement of Seebeck coefficient for Bi_2Se_3 is less obvious. However, 2% tensile strain can increase the magnitude of S in n -doped Bi_2Se_3 for electron concentrations of $2 \times 10^{18}\text{cm}^{-3} - 10^{20}\text{cm}^{-3}$. For comparison, we have also computed the thermoelectric properties of corresponding PBE + SOC optimized structures. The predicted thermoelectric properties can be *qualitatively* different, as shown in Figs. 7(c) and 7(d), therefore underscoring the importance of vdW interactions in structural optimization and in predicting the effects of strain on electronic and thermoelectric properties. In the following, we focus on vdW-DF^{C09}_x relaxed structures.

Figure 8 depicts the temperature dependence of the Seebeck coefficient S under different in-plane strains, with the carrier concentration fixed to 10^{19}cm^{-3} . Figure 8(a) shows that compressive strain can increase the Seebeck coefficient of p -doped Bi_2Te_3 when the temperature is higher than 350 K, and the peak value can be shifted from 300 to 400 K when a 3% compressive strain is applied. This result is very similar to the

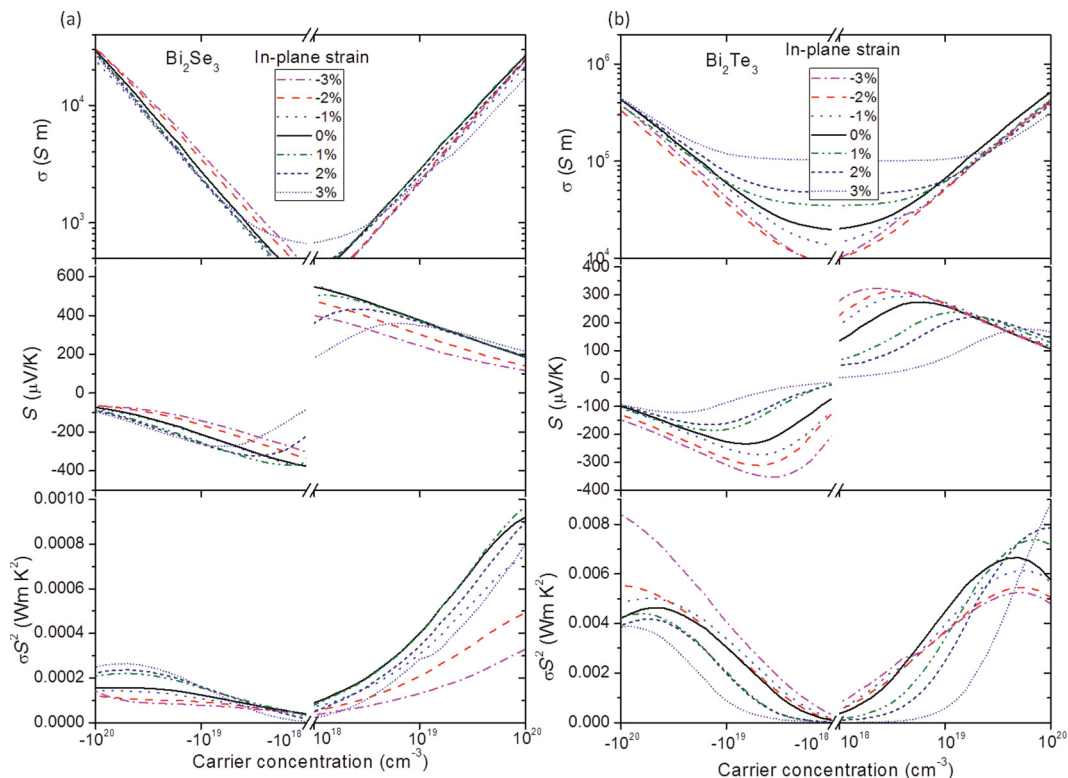


FIG. 9. (Color online) The conductivity, Seebeck coefficient and power factor of (a) Bi_2Se_3 and (b) Bi_2Te_3 under different in-plane strains. Negative-carrier concentrations denote electron doping. The power factor of Bi_2Se_3 is an order of magnitude smaller than that of Bi_2Te_3 , because of its much smaller conductivity.

prediction of Ref. 76, in which the authors changed the lattice constants of Bi_2Te_3 to that of Sb_2Te_3 to model a compressive in-plane strain. Overall, the strain does not improve the p -type Seebeck coefficient of Bi_2Se_3 , except for a small enhancement at temperatures higher than 500 K [Fig. 8(b)]. As noted before, the p -type Seebeck coefficient, in general, is larger in Bi_2Se_3 than in Bi_2Te_3 , reaching about $400 \mu\text{V/K}$ at 350 K.

On the other hand, compressive strain increases the magnitude of the Seebeck coefficient in n -doped Bi_2Te_3 for all temperatures considered here, and the maximum of the Seebeck coefficient is shifted to higher temperature with larger compressive strain [Fig. 8(c)]. Most notably, under 3% compressive strain, the magnitude of the Seebeck coefficient reaches a maximum of $305 \mu\text{V/K}$ at 350 K, roughly 45% higher than that of unstrained Bi_2Te_3 ($210 \mu\text{V/K}$) at the same temperature. For n -doped Bi_2Se_3 , compressive strains instead reduce the magnitude of the Seebeck coefficient, but tensile strain increases this magnitude for temperatures less than ~ 500 K [Fig. 8(d)]. Furthermore, the maximum magnitude of the Seebeck coefficient is shifted to lower temperatures at larger tensile strains. A maximum magnitude of $256 \mu\text{V/K}$ is achieved in the Seebeck coefficient of Bi_2Se_3 under 1% tensile strain, 13% larger than the maximum magnitude in the unstrained system. It is interesting to note that under 2% tensile strain, the maximum magnitude of Seebeck coefficient of n -type Bi_2Se_3 ($252 \mu\text{V/K}$) is at about 350 K, the same temperature where n -type Bi_2Te_3 has the largest Seebeck coefficient under 3% compressive strain. Since the in-plane lattice constant of Bi_2Se_3 is about 5%

smaller than that of Bi_2Te_3 , it is possible that in a superlattice structure, the tensile strain in Bi_2Se_3 and compressive strain on Bi_2Te_3 result in a larger Seebeck coefficient. Together with the reduced lattice thermal conductivity in a superlattice structure, this may greatly improve the thermoelectric performance.

The electrical conductivity σ can be readily calculated within the constant relaxation-time approximation given an estimate for the relaxation time τ . In practice, we can estimate τ by comparing our computed values of σ/τ and S for unstrained systems, with experimentally^{74,79} measured values of σ and S at the same temperature (300 K), as described in Ref. 44. In this way, in-plane relaxation times of 2.2×10^{-14} s and 2.7×10^{-15} s are derived for Bi_2Te_3 and Bi_2Se_3 , respectively. In Ref. 44, it was shown that this derived relaxation time for Bi_2Te_3 gives good agreement with experiment for different doping concentrations; here, we further assume that the relaxation time is independent of strain, as is also assumed by other authors.³⁷

The resulting conductivities and power factors (at 300 K) are plotted in Fig. 9 for different in-plane strains (positive- and negative-carrier concentrations denote the p -type and n -type doping, respectively). The conductivity of Bi_2Te_3 is 20 times larger than that of Bi_2Se_3 ; this is consistent with the physical picture that Bi_2Te_3 has a smaller bandgap. Strain has a significantly larger effect on the conductivity of Bi_2Te_3 than Bi_2Se_3 . Tensile strain increases the conductivity while compressive strain decreases the conductivity in Bi_2Te_3 , for both p -type and n -type doping, an observation that is consistent with the

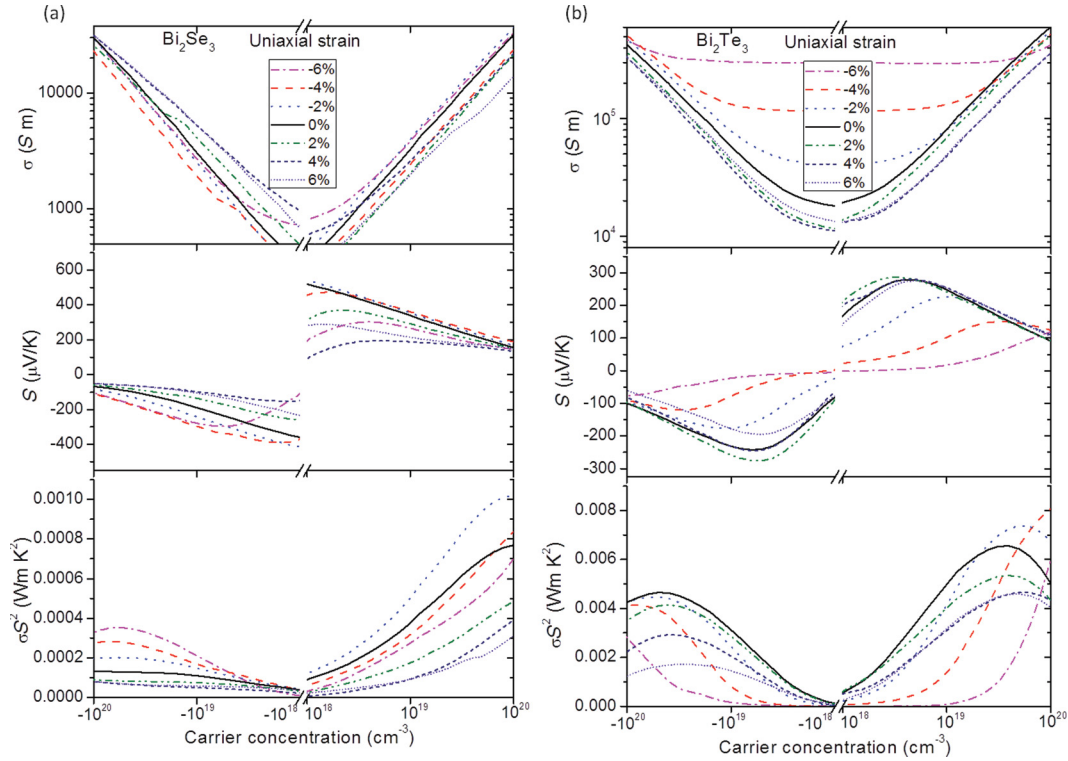


FIG. 10. (Color online) The conductivity, Seebeck coefficient and power factor of (a) Bi_2Se_3 and (b) Bi_2Te_3 under different uniaxial strains. Negative-carrier concentrations denote electron doping.

increase in bandgap from tensile to compressive strain. The Seebeck coefficient is related with the conductivity and the electron-hole asymmetry. When $E - \mu \gg k_B T$, Eq. (2) can be expressed in the Mott formulas,⁸⁰

$$S = \left(\frac{\pi^2 k_B^2 T}{3e\sigma} \right) \frac{d\sigma}{dE} \Big|_{E=E_F} = \frac{\pi^2 k_B^2 T}{3e} \frac{d \ln \sigma}{dE} \Big|_{E=E_F}. \quad (5)$$

Therefore, we can understand the Seebeck coefficient from the energy derivative of the log-scale conductivity. By comparing the conductivity and Seebeck coefficients in Figs. 9(a) and 9(b), we find that qualitatively, the carrier concentration can be used as an approximate proxy for the energy scale—the Seebeck coefficient is larger when the slope of the conductivity curve is steeper. This is also consistent with the increased Seebeck coefficients with compressive strain for Bi_2Te_3 . We further note that although the Seebeck coefficient of Bi_2Se_3 is in general larger than that of Bi_2Te_3 , under compressive strain, the n -type Seebeck coefficient of Bi_2Te_3 can surpass that of Bi_2Se_3 . This large enhancement in n -type Seebeck coefficient of Bi_2Te_3 with compressive strain is in agreement with Ref. 77. Finally, we computed the power factor for Bi_2Se_3 and Bi_2Te_3 under different strain states. The power factor for Bi_2Te_3 is one order of magnitude larger than that for Bi_2Se_3 , due to the much larger conductivity in Bi_2Te_3 . Although the compressive strains can reduce the electron conductivity of n -type Bi_2Te_3 , it will also increase its Seebeck coefficient. The larger enhancement of the Seebeck coefficient makes it possible to compensate the reduction of conductivity, resulting in an enhancement of the n -type power factor for Bi_2Te_3 , under compressive in-plane strain.

This result is different from that in Ref. 77—the discrepancy may come from the different methods for imposing strain (in Ref. 77, the strain is imposed by setting the in-plane and out-of-plane lattice constants of Bi_2Te_3 to that of Sb_2Te_3 , without relaxing the internal coordinates).

Finally, we show in Fig. 10 the thermoelectric properties of Bi_2Se_3 and Bi_2Te_3 under uniaxial strain. In contrast to the case for in-plane strain, tensile uniaxial strain decreases the conductivity, and compressive uniaxial strain increases the conductivity for Bi_2Te_3 , while tensile uniaxial strain increases Seebeck coefficient slightly, and compressive strain decreases Seebeck coefficient. Unlike the case of in-plane strain, these opposite effects on Seebeck coefficient and conductivity result in no enhancement of the power factor for Bi_2Te_3 under compressive uniaxial strain. Uniaxial strain can be used to enhance the power factor of Bi_2Se_3 , however, compressive strain enhances the n -type power factor because of an increased magnitude of Seebeck coefficient (the power factor more than doubles under compressive uniaxial strain of 4–6%, for doping concentrations between 10^{19} and 10^{20} cm^{-3}), while 2% compressive uniaxial strain can enhance the p -type power factor.

IV. CONCLUSION

In summary, we have performed a comprehensive investigation of the effects of strain on the atomic, electronic, and thermoelectric properties of Bi_2Se_3 and Bi_2Te_3 , taking into account the vdW interlayer interactions using the vdW-DF^{C09}_x functional. Our optimized, unstrained structures are in much closer agreement with the experimental structure from Nakajima (determined by x-ray diffraction) than with

that from Wyckoff (determined by electron diffraction).^{58,59} Importantly, the two experimental structures have qualitatively different band structures on Bi₂Se₃—previously published photoemission results⁶¹ on Bi₂Se₃ are in good qualitative agreement with the band structure of vdW-DF^{C09}_x optimized structure and the Nakajima structure, but not the Wyckoff structure, and the Γ -point bandgap for the vdW-DF^{C09}_x optimized Bi₂Se₃ thin films closes at four QLs instead of three QLs, as previously reported using the Wyckoff structure. We predict that the bandgaps of these materials increase from tensile to compressive in-plane strain, suggesting that compressive strain may be used to increase the bulk bandgap of Bi₂Se₃, thus making it easier to distinguish the metallic topological surface state from intrinsic bulk carriers. We also confirm that a topological phase transition can occur in Bi₂Se₃ at 6% uniaxial strain, as predicted by Young *et al.*²⁸ Strain can also be used to tune the thermoelectric properties of these materials: the *n*-type Seebeck coefficient of Bi₂Te₃ can be increased by compressive in-plane strain while that of Bi₂Se₃ can be increased with tensile in-plane strain. The power factor

of *n*-doped Bi₂Se₃ can be increased with compressive uniaxial strain while that of *n*-doped Bi₂Te₃ can be increased by compressive in-plane strain. Finally, we have compared the properties of structures optimized using different functionals and found that taking into account vdW interactions is crucial for the predictions of electronic and thermoelectric properties of strained structures, while spin-orbit interactions are less important for structure determination. In contrast, calculations on phonon frequencies suggest that SOC is important for accurate predictions of frequencies, while it is unclear if vdW methods, as currently implemented, contribute to accurate predictions of frequencies.

ACKNOWLEDGMENTS

This work was supported by the IHPC Independent Investigatorship (I³) program. The authors acknowledge the support from the A*STAR Computational Resource Center and early discussions with O. Yazyev. The authors also thank C. K. Gan for the phonon code (force constant approach).

*queksy@ihpc.a-star.edu.sg

- ¹D. Kraemer, B. Poudel, H. P. Feng, J. C. Caylor, B. Yu, X. Yan, Y. Ma, X. Wang, D. Wang, and A. Muto, *Nat. Mater.* **10**, 532 (2011).
- ²I. Chowdhury, R. Prasher, K. Lofgreen, G. Chrysler, S. Narasimhan, R. Mahajan, D. Koester, R. Alley, and R. Venkatasubramanian, *Nature Nanotechnol.* **4**, 235 (2009).
- ³R. Venkatasubramanian, E. Siivola, T. Colpitts, and B. O'Quinn, *Nature (London)* **413**, 597 (2001).
- ⁴L. Fu, C. L. Kane, and E. J. Mele, *Phys. Rev. Lett.* **98**, 106803 (2007).
- ⁵Y. Xia, D. Qian, D. Hsieh, L. Wray, A. Pal, H. Lin, A. Bansil, D. Grauer, Y. S. Hor, R. J. Cava, and M. Z. Hasan, *Nat. Phys.* **5**, 398 (2009).
- ⁶Y. L. Chen, J. G. Analytis, J. H. Chu, Z. K. Liu, S. K. Mo, X. L. Qi, H. J. Zhang, D. H. Lu, X. Dai, and Z. Fang, *Science* **325**, 178 (2009).
- ⁷H. Zhang, C. X. Liu, X. L. Qi, X. Dai, Z. Fang, and S. C. Zhang, *Nat. Phys.* **5**, 438 (2009).
- ⁸M. Z. Hasan and C. L. Kane, *Rev. Mod. Phys.* **82**, 3045 (2010).
- ⁹J. E. Moore, *Nature (London)* **464**, 194 (2010).
- ¹⁰X.-L. Qi and S.-C. Zhang, *Rev. Mod. Phys.* **83**, 1057 (2011).
- ¹¹M. Bianchi, R. C. Hatch, J. Mi, B. B. Iversen, and P. Hofmann, *Phys. Rev. Lett.* **107**, 086802 (2011).
- ¹²H. M. Benia, C. T. Lin, K. Kern, and C. R. Ast, *Phys. Rev. Lett.* **107**, 177602 (2011).
- ¹³O. V. Yazyev, J. E. Moore, and S. G. Louie, *Phys. Rev. Lett.* **105**, 266806 (2010).
- ¹⁴M. Z. Hasan and J. E. Moore, *Annu. Rev. Condens. Matter Phys.* **2**, 55 (2011).
- ¹⁵P. Ghaemi, R. S. K. Mong, and J. E. Moore, *Phys. Rev. Lett.* **105**, 166603 (2010).
- ¹⁶T. Sato and H. Nakai, *J. Chem. Phys.* **131**, 224104 (2009).
- ¹⁷E. R. Johnson, I. D. Mackie, and G. A. DiLabio, *J. Phys. Org. Chem.* **22**, 1127 (2009).
- ¹⁸S. Grimme, J. Antony, S. Ehrlich, and H. Krieg, *J. Chem. Phys.* **132**, 154104 (2010).

- ¹⁹M. Dion, H. Rydberg, E. Schroder, D. C. Langreth, and B. I. Lundqvist, *Phys. Rev. Lett.* **92**, 246401 (2004).
- ²⁰T. Thonhauser, V. R. Cooper, S. Li, A. Puzder, P. Hyldgaard, and D. C. Langreth, *Phys. Rev. B* **76**, 125112 (2007).
- ²¹Y. Zhang and W. Yang, *Phys. Rev. Lett.* **80**, 890 (1998).
- ²²D. Langreth, B. I. Lundqvist, S. D. Chakarova-Käck, V. Cooper, M. Dion, P. Hyldgaard, A. Kelkkanen, J. Kleis, L. Kong, and S. Li, *J. Phys.: Condens. Matter* **21**, 084203 (2009).
- ²³V. R. Cooper, *Phys. Rev. B* **81**, 161104 (2010).
- ²⁴S. K. Mishra, S. Satpathy, and O. Jepsen, *J. Phys.: Condens. Matter* **9**, 461 (1997).
- ²⁵P. Larson, S. D. Mahanti, and M. G. Kanatzidis, *Phys. Rev. B* **61**, 8162 (2000).
- ²⁶P. Larson, V. A. Greanya, W. C. Tonjes, R. Liu, S. D. Mahanti, and C. G. Olson, *Phys. Rev. B* **65**, 085108 (2002).
- ²⁷G. Wang and T. Cagin, *Phys. Rev. B* **76**, 075201 (2007).
- ²⁸S. M. Young, S. Chowdhury, E. J. Walter, E. J. Mele, C. L. Kane, and A. M. Rappe, *Phys. Rev. B* **84**, 085106 (2011).
- ²⁹N. F. Hinsche, B. Y. Yavorsky, I. Mertig, and P. Zahn, *Phys. Rev. B* **84**, 165214 (2011).
- ³⁰W. Zhang, R. Yu, H. J. Zhang, X. Dai, and Z. Fang, *New J. Phys.* **12**, 065013 (2010).
- ³¹Y. Zhao, Y. Hu, L. Liu, Y. Zhu, and H. Guo, *Nano Lett.* **11**, 2088 (2011).
- ³²H. Chen, W. Zhu, D. Xiao, and Z. Zhang, *Phys. Rev. Lett.* **107**, 056804 (2011).
- ³³M. Ye, S. V. Eremeev, K. Kuroda, M. Nakatake, S. Kim, Y. Yamada, E. E. Krasovskii, E. V. Chulkov, M. Arita, and H. Miyahara, e-print arXiv:1112.5869 (unpublished).
- ³⁴C. Brune, C. X. Liu, E. G. Novik, E. M. Hankiewicz, H. Buhmann, Y. L. Chen, X. L. Qi, Z. X. Shen, S. C. Zhang, and L. W. Molenkamp, *Phys. Rev. Lett.* **106**, 126803 (2011).
- ³⁵J. L. Zhang, S. J. Zhang, H. M. Weng, W. Zhang, L. X. Yang, Q. Q. Liu, S. M. Feng, X. C. Wang, R. C. Yu, and L. Z. Cao, *Proc. Natl. Acad. Sci. USA* **108**, 24 (2011).

- ³⁶T. Thonhauser, T. J. Scheidemantel, J. O. Sofo, J. V. Badding, and G. D. Mahan, *Phys. Rev. B* **68**, 085201 (2003).
- ³⁷T. Thonhauser, G. S. Jeon, G. D. Mahan, and J. O. Sofo, *Phys. Rev. B* **68**, 205207 (2003).
- ³⁸T. Thonhauser, *Solid State Commun.* **129**, 249 (2004).
- ³⁹M. T. Alam, M. P. Manoharan, M. A. Haque, C. Muratore, and A. Voevodin, *J. Micromech. Microeng.* **22**, 045001 (2012).
- ⁴⁰X. Li, K. Maute, M. L. Dunn, and R. Yang, *Phys. Rev. B* **81**, 245318 (2010).
- ⁴¹A. Dal Corso and A. Mosca Conte, *Phys. Rev. B* **71**, 115106 (2005).
- ⁴²M. V. Fischetti, Z. Ren, P. M. Solomon, M. Yang, and K. Rim, *J. Appl. Phys.* **94**, 1079 (2003).
- ⁴³J. P. Perdew, K. Burke, and M. Ernzerhof, *Phys. Rev. Lett.* **77**, 3865 (1996).
- ⁴⁴T. J. Scheidemantel, C. Ambrosch-Draxl, T. Thonhauser, J. V. Badding, and J. O. Sofo, *Phys. Rev. B* **68**, 125210 (2003).
- ⁴⁵G. K. H. Madsen and D. J. Singh, *Comput. Phys. Commun.* **175**, 67 (2006).
- ⁴⁶D. Parker and D. J. Singh, *Phys. Rev. X* **1**, 021005 (2011).
- ⁴⁷P. Blaha, K. Schwarz, P. Sorantin, and S. B. Trickey, *Comput. Phys. Commun.* **59**, 399 (1990).
- ⁴⁸B. R. Nag, *Electron Transport in Compound Semiconductors* (Springer-Verlag, Berlin, 1980).
- ⁴⁹A. H. MacDonald, W. E. Pickett, and D. D. Koelling, *J. Phys. C* **13**, 2675 (1980).
- ⁵⁰J. P. Perdew and Y. Wang, *Phys. Rev. B* **45**, 13244 (1992).
- ⁵¹S. Grimme, *J. Comput. Chem.* **27**, 1787 (2006).
- ⁵²V. Barone, M. Casarin, D. Forrer, M. Pavone, M. Sami, and A. Vittadini, *J. Comput. Chem.* **30**, 934 (2009).
- ⁵³G. Román-Pérez and J. M. Soler, *Phys. Rev. Lett.* **103**, 096102 (2009).
- ⁵⁴P. H. Tan, W. P. Han, W. J. Zhao, Z. H. Wu, K. Chang, H. Wang, Y. F. Wang, N. Bonini, N. Marzari, and N. Pugno, *Nat. Mater.* **11**, 294 (2012).
- ⁵⁵Y. Y. Zhao, X. Luo, H. Li, J. Zhang, P. A. Trindade Araujo, C. K. Gan, H. Zhang, S. Y. Quek, M. S. Dresselhaus, and Q. H. Xiong, (unpublished).
- ⁵⁶O. A. Vydrov and T. Van Voorhis, *J. Chem. Phys.* **133**, 244103 (2010).
- ⁵⁷T. Bjorkman, A. Gulans, A. V. Krasheninnikov, and R. M. Nieminen, *Phys. Rev. Lett.* **108**, 235502 (2012).
- ⁵⁸S. Nakajima, *J. Phys. Chem. Solids* **24**, 479 (1963).
- ⁵⁹W. G. Wyckoff, *Crystal Structures* (Wiley-Interscience, New York, 1964).
- ⁶⁰S. A. Semiletov, *Tr. Inst. Kristallogr., Akad. Nauk SSSR* **10**, 76 (1954).
- ⁶¹V. A. Greanya, W. C. Tonjes, R. Liu, C. G. Olson, D. Y. Chung, and M. G. Kanatzidis, *J. Appl. Phys.* **92**, 6658 (2002).
- ⁶²M. S. Hybertsen and S. G. Louie, *Phys. Rev. B* **34**, 5390 (1986).
- ⁶³J. Black, E. M. Conwell, L. Seigle, and C. W. Spencer, *J. Phys. Chem. Solids* **2**, 240 (1957).
- ⁶⁴O. V. Zazyev, E. Kioupakis, J. E. Moore, and S. G. Louie, *Phys. Rev. B* **85**, 161101 (2012).
- ⁶⁵C. X. Liu, H. J. Zhang, B. Yan, X. L. Qi, T. Frauenheim, X. Dai, Z. Fang, and S. C. Zhang, *Phys. Rev. B* **81**, 041307 (2010).
- ⁶⁶Y. Zhang, K. He, C. Z. Chang, C. L. Song, L. L. Wang, X. Chen, J. F. Jia, Z. Fang, X. Dai, and W. Y. Shan, *Nat. Phys.* **6**, 584 (2010).
- ⁶⁷R. Vilaplana, D. Santamaría-Pérez, O. Gomis, F. J. Manjón, J. González, A. Segura, A. Muñoz, P. Rodríguez-Hernández, E. Pérez-González, V. Marín-Borrás, V. Muñoz-Sanjose, C. Drasar, and V. Kucek, *Phys. Rev. B* **84**, 184110 (2011).
- ⁶⁸M. Lazzeri and F. Mauri, *Phys. Rev. Lett.* **90**, 036401 (2003).
- ⁶⁹C. K. Gan, Y. P. Feng, and D. J. Srolovitz, *Phys. Rev. B* **73**, 235214 (2006).
- ⁷⁰G. Kresse, J. Furthmüller, and J. Hafner, *Europhys. Lett.* **32**, 729 (2007).
- ⁷¹W. Cheng and S. F. Ren, *Phys. Rev. B* **83**, 094301 (2011).
- ⁷²H. J. Goldsmid and R. W. Douglas, *Br. J. Appl. Phys.* **5**, 386 (1954).
- ⁷³H. J. Goldsmid, *Proc. Phys. Soc. London* **71**, 633 (1958).
- ⁷⁴H. J. Goldsmid, A. R. Sheard, and D. A. Wright, *Br. J. Appl. Phys.* **9**, 365 (1958).
- ⁷⁵T. M. Tritt, *Annu. Rev. Mater. Res.* **41**, 433 (2011).
- ⁷⁶M. S. Park, J.-H. Song, J. E. Medvedeva, M. Kim, I. G. Kim, and A. J. Freeman, *Phys. Rev. B* **81**, 155211 (2010).
- ⁷⁷B. Y. Yavorsky, N. F. Hinsche, I. Mertig, and P. Zahn, *Phys. Rev. B* **84**, 165208 (2011).
- ⁷⁸We note that the band structures obtained from WIEN2k are slightly different from that obtained with QE. This difference may be due to the different implementations of spin-orbit coupling in the two codes.
- ⁷⁹Y. S. Hor, A. Richardella, P. Roushan, Y. Xia, J. G. Checkelsky, A. Yazdani, M. Z. Hasan, N. P. Ong, and R. J. Cava, *Phys. Rev. B* **79**, 195208 (2009).
- ⁸⁰N. F. Mott and E. A. Davis, *Electronic Processes in Non-Crystalline Materials* (Clarendon, Oxford, 1979).
- ⁸¹J. J. Hamlin, J. R. Jeffries, N. P. Butch, P. Syers, D. A. Zocco, S. T. Weir, Y. K. Vohra, J. Paglione, and M. B. Maple, *J. Phys.: Condens. Matter* **24**, 035602 (2011).
- ⁸²J. O. Jenkins, J. A. Rayne, and R. W. Ure, Jr., *Phys. Rev. B* **5**, 3171 (1972).
- ⁸³R. Vilaplana, O. Gomis, F. J. Manjón, A. Segura, E. Pérez-González, P. Rodríguez-Hernández, A. Muñoz, J. González, V. Marín-Borrás, V. Muñoz-Sanjose, C. Drasar, and V. Kucek, *Phys. Rev. B* **84**, 104112 (2011).
- ⁸⁴J. Zhang, Z. Peng, A. Soni, Y. Zhao, Y. Xiong, B. Peng, J. Wang, M. S. Dresselhaus, and Q. Xiong, *Nano Lett.* **11**, 2407 (2011).
- ⁸⁵K. M. F. Shahil, M. Z. Hossain, D. Teweldebrhan, and A. A. Balandin, *Appl. Phys. Lett.* **96**, 153103 (2010).